Physics of Fluids

An experimental study on the transient runback characteristics of wind-driven film/rivulet flows

Cite as: Phys. Fluids **33**, 112104 (2021); https://doi.org/10.1063/5.0067672
Submitted: 18 August 2021 • Accepted: 20 October 2021 • Published Online: 03 November 2021

Kai Zhang and Hui Hu

Physics of Fluids ARTICLE scitation.org/journal/phf

An experimental study on the transient runback characteristics of wind-driven film/rivulet flows

Cite as: Phys. Fluids 33, 112104 (2021); doi: 10.1063/5.0067672
Submitted: 18 August 2021 · Accepted: 20 October 2021 ·
Published Online: 3 November 2021

View Online Export Citation CrossMark

Kai Zhang and Hui Hu[a)]

AFFILIATIONS

Department of Aerospace Engineering, Iowa State University, Ames, Iowa 50011-1096, USA

[a)]Author to whom correspondence should be addressed: huhui@iastate.edu

ABSTRACT

A comprehensive experimental campaign was conducted to characterize the dynamic runback process of wind-driven water film/rivulet flows for a better understanding of the transient surface water transport process pertinent to aircraft icing phenomena. The experimental study was conducted by using an open-circuit wind tunnel to generate laminar boundary layer airflows with different freestream wind speeds to drive thin water film/rivulet flows over a flat test plate. A digital image projection (DIP) technique was used to achieve non-intrusive, temporally and spatially resolved measurements of the film thickness distributions to characterize the dynamic runback process of the wind-driven film/rivulet flow under different test conditions. Important characteristics of the wind-driven water runback process—such as the generation of well-organized two-dimensional (i.e., 2D) and more complicated three-dimensional (i.e., 3D) surface waves at air/water interfaces, stumbling runback motion of the film/rivulet heads in "acceleration-and-deceleration" cycles, breaking up the front contact lines to form multiple rivulet flows, meandering and merging of the rivulet flows—were revealed clearly and quantitatively based on the DIP measurements. A comprehensive force balance analysis was also performed to examine the variations of the relevant forces (i.e., the excess pressure forces built inside the film/rivulet flows, aerodynamic drag forces acting on the rivulet heads, and the restraining forces due to the surface tension along the liquid contact lines) and evaluate their importance in the breakoff of the stagnated film/rivulet heads to re-start the runback process of the wind-driven film/rivulet flows.

I. INTRODUCTION

Aircraft icing is a well-known weather hazard affecting flight safety and performance. As an airplane flies under cold weather conditions, supercooled water droplets in the clouds would impinge, freeze, and form ice shapes on airframe surfaces.[1,2] The ice accretion process over airframe surfaces can be either a dry rime or wet glaze icing process, highly depending on the weather conditions, including the cloud liquid water content (LWC), atmosphere temperature, and size of the supercooled water droplets in the cloud.[3,4] Under a typical glaze icing condition with relatively warm ambient temperatures (e.g., just below the freezing point of water), higher LWC levels in the cloud, and larger supercooled water droplets, while only a portion of the impacted supercooled water droplets would be frozen into solid ice instantly upon impacting onto airframe surfaces, the rest of the impacted water would stay in the liquid and run back freely over the airframe surfaces, as driven by boundary layer airflows.[3,5,6] The runback behavior of unfrozen water film/rivulet flows on airframe surfaces can directly and indirectly influence the resultant shape of ice accretion.[7] While the transport process of the unfrozen water would have a direct impact on the formation of the final ice shape due to its effect on the redistribution of the impinged water mass over airframe surfaces,[8] it would also be able to influence the ice accretion process through its impacts on the surface roughness, thereby, affecting the local convective heat transfer and the ice accretion rate over the airframe surfaces.[9–12] Hansman and Turnock[13] conducted an experimental study to examine the importance of surface water transport on the glaze ice accretion process, and confirmed that the wind-driven runback process of unfrozen water would alter the final glaze ice shape significantly. Waldman and Hu[14] visualized the dynamic glaze ice accretion process on an airfoil surface with a high-speed imaging system, and revealed that the stagnated rivulet fronts/heads would act as barriers to block the surface water transport, thereby, affecting the ice accretion process over the airfoil/wing surface.

While the dynamics of thin film flows under the influence of external fields—such as gravitational,[15] electric,[16,17] and temperature[18,19] fields—have been investigated comprehensively in recent years, the present study aims to provide fundamental insights into the dynamics of wind-driven film/rivulet flows and its effects on the

surface water transport process pertinent to aircraft icing phenomena. It should be noted that several fundamental studies have already been conducted to elucidate the underlying physics associated with the dynamics of water film/rivulet flows over solid surfaces. For example, Hartley and Murgatroyd[20] conducted a theoretical study to predict the re-wetting process of surface shear-driven thin film/rivulet flows over solid surfaces. They established two film breakup criteria to predict the minimum film thickness required for re-wetting a dry patch that occurs when the excess pressure force built inside a film flow surpasses the restraining surface tension force at the stagnation point: one is based on the force balance (FB) analysis near the stagnation point of a dry patch; the other is based on the minimization of total energy (MTE) of a stable rivulet. Murgatroyd[21] refined the FB model by adding the unbalanced shear stress between the solid–liquid and liquid–gas interfaces. A characteristic length was introduced to represent the length of the unbalanced shear stress range. The unbalanced shear stress length was determined by fitting the experimental data empirically. Penn *et al.*[22] determined the unbalanced shear stress length via CFD simulation. El-Genk and Sable[23] refined the MTE model by considering the velocity distribution within film/rivulet flows. The velocity profile was estimated numerically by using a finite element method (FEM) for a more accurate prediction of the kinetic energy of the film/rivulet flow. The refined MTE model was then applied to predict the minimum film thickness of a falling film flow on a vertical surface. The method suggested by El-Genk and Sable[23] was further extended to determine the breakoff of the stagnated film flow subject to interfacial shear.[24]

Both FB and MTE criteria were also adopted to study aircraft icing phenomena. Thompson and Marrochello[25] used a FB criterion to predict the rivulet formation of wind-driven water runback flows over a NACA4412 airfoil surface. Al-Khalil *et al.*[26] developed a water runback model based on the MTE criterion for aircraft icing applications. It should be noted that the stagnated rivulet head or dry patch was usually treated as a smooth flat surface for FB analysis in those previous studies. However, in reality, for wind-driven water film/rivulet flows pertinent to aircraft icing phenomena, smooth rivulet fronts would exist only when the incoming wind speed is very low (i.e., not high enough to induce surface waves at the air/water interfaces).[27] In general, the surface waves generated at the air/water interfaces would induce the formation of hump-shaped rivulet fronts/heads, consequently, leading to additional aerodynamic drag forces, which were not considered in the original FB analysis. The additional aerodynamic drag forces could be very substantial, even becoming dominant, in comparison to the restraining forces due to the surface tension. Thompson and Marrochello[25] and McAlister *et al.*[28] modified the original FB model by taking the additional aerodynamic drag forces into account in predicting the rivulet breakoff for wind-driven film/rivulet flows; however, a very simplified model was used in estimating the aerodynamic drag forces acting on the rivulet fronts/heads. Due to lack of accurate measurement techniques to quantify the transient behavior of wind-driven film/rivulet flows, many important runback characteristics of wind-driven water film/rivulet flows are still unclear.

In the present study, we report a comprehensive experimental campaign to characterize the transient behavior of water film/rivulet flows driven by boundary layer airflows over a flat plate for a better understanding of the surface water transport process pertinent to aircraft icing phenomena. The experimental study was conducted by using an open-circuit wind tunnel to generate laminar boundary layer airflows with different freestream wind speeds to drive thin water film flows over a flat test plate with different water flow rates. A novel digital image projection (DIP) system[29,30] was applied to provide non-intrusive, temporally and spatially resolved measurements of the thickness distributions of the wind-driven water film/rivulet flows over the flat plate. The measured film thicknesses distributions of the wind-driven water film/rivulet flows were further processed to determine the instantaneous runback velocity of the rivulet fronts/heads under different test conditions. A comprehensive force balance (FB) analysis was also performed to examine the variations of the relevant forces (i.e., the excess pressure forces built inside the film/rivulet flows, aerodynamic drag forces acting on the rivulet heads, and the restraining forces due to surface tension along the liquid contact lines) and to evaluate their importance in determining the runback characteristics of the wind-driven film/rivulet flows.

II. EXPERIMENTAL SETUP AND MEASUREMENT TECHNIQUES

A. Experimental setup

The experimental study was performed in an open-circuit, low-speed wind tunnel available at the Aerospace Engineering Department of Iowa State University. The wind tunnel has a test section with a dimension of 200 mm × 150 m× 500 m (width × height × length) and four optically transparent walls. Figure 1 shows the experimental setup used to quantify the dynamic runback process of wind-driven water film/rivulet flows over a flat test plate. As shown schematically in Fig. 1, a flat test plate, which is 250 mm in length and 150 mm in width, is made of a hard plastic material (i.e., VeroWhitePlus, RGD835) and manufactured by using a rapid prototyping machine (i.e., Stratasys 3D printer). The upper surface of the test plate was polished with fine sandpaper (i.e., up to 2000 grit) and special plastic polishes to achieve a very smooth, glossy finish. During the experiments,

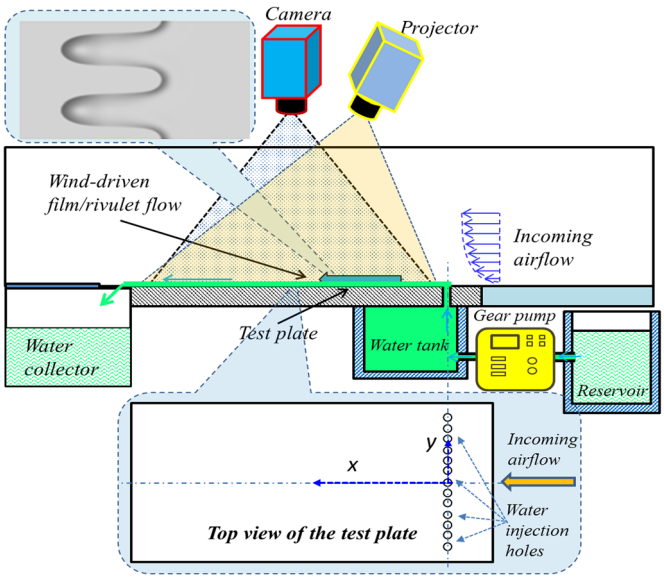

FIG. 1. Experimental setup used to study wind-driven water film/rivulet flows.

the test plate was flush mounted to the bottom wall of the wind tunnel test section. Thirteen water outlet holes were uniformly distributed near the entrance of the test plate. A digital gear pump (Cole-Parmer 75211–30) was used to drive water from a reservoir to go through the water injection holes to form a water film over the test plate. While the diameter of the water injection holes is 2.0 mm, the distance between the neighboring holes is 5.0 mm. As a result, the nominal width of the water film over the test plate is $D = 60$ mm. The flow rate of the water film flow was controlled by adjusting the settings of the digital gear pump and monitored by using a digital flowmeter (Omega FLR 1010 T-D). After exhausted from the water injection holes, the water film would run back over the test plate as driven by the boundary layer airflow.

It was found that surface water runback processes over ice accreting airframe surfaces would be conducted in different modes, depending on the speed of the incoming airflow and the thickness of the water film over the surface. As described in Liu *et al.*,[27] the evolution of the instability at the air/water interface of a wind-driven film flow could be categorized into three regimes: (1) no obvious surface wave generation at the air/water interface when the incoming wind speed is relatively low (i.e., $U_\infty < 10$ m/s); (2) formation of well-organized, two-dimensional surface waves at medium wind speeds (i.e., $10 < U_\infty < 15$ m/s); and (3) formation of complex three-dimensional surface waves when the incoming wind speed is sufficiently high (i.e., $U_\infty > 15$ m/s). In order to examine the effects of surface waves generated at the air/water interfaces on the characteristics of wind-driven film/rivulet flows in different flow regimes, the freestream speed of the incoming airflows over the test plate was changed from $U_\infty = 5$ to $U_\infty = 20$ m/s for different test cases. Following up the work of Liu *et al.*,[27] the flow rates of the water flow injected onto the test plate were set to be $Q = 100$ and 200 ml/min during the experiments.

Before injecting water mass over the test plate, a high-resolution digital particle image velocimetry (PIV) system was used to characterize the boundary layer airflow over the test plate. Figure 2 shows some typical PIV measurement results (i.e., time-averaged velocity profiles) at the center of the test plate (i.e., at 100 mm downstream of the water injection holes). Before the injection of water film over the test plate, the velocity profiles of the boundary layer airflows at the center of the test section were found to be fit well by Blasius solution.[31] After injecting water over the test plate, a thin water film/rivulet flow would form over the test plate. It should be noted that, while wavy surface waves were found to be generated at the air/water interface for the test cases with relatively high incoming wind speeds (i.e., $U_\infty > 15$ m/s), since the thickness of the wind-driven film/rivulet flow over the test plate is very thin (i.e., being less than 1.0 mm), the characteristics of the boundary layer airflows over the test plate were found to be almost unchanged in comparison to those shown in Fig. 2. Therefore, the water film/rivulet flows over the test plate are assumed to be driven by laminar boundary layer winds for the test cases of the present study.

B. Digital image projection (DIP) technique

A digital image projection (DIP) system was used in the present study to achieve time-resolved measurements of the thickness distributions of the water film over the test plate in order to quantify the transient runback behavior of the wind-driven water film/rivulet flows. As described in Zhang *et al.*,[30] the DIP technique is based on the principle of structured light triangulation in a fashion similar to a stereo vision technique, but replacing one of the cameras for stereoscopic imaging with a digital projector. A Dell DLP projector (M109S) was used to in the present study to project a grid pattern onto the test plate. The projected digital images have 7 ×7 pixel grids, corresponding to about 1.0 × 1.0 mm in the physical domain over the test plate. A digital camera was used to acquire images of the projected grids over the test surface. The frame rate of the digital camera was set to 30.0 Hz with 2.0 ms exposure time. The digital camera and the projector were synchronized by using a digital delay generator. A DIP measurement window was selected to locate right downstream of the water injection holes with approximately 100 × 60 mm in size. The DIP reference images were acquired without having water film/rivulet on the test plate. After switching on the gear pump to inject water onto the test plate, 600 frames (i.e., with a time duration of 20 s) of the projected

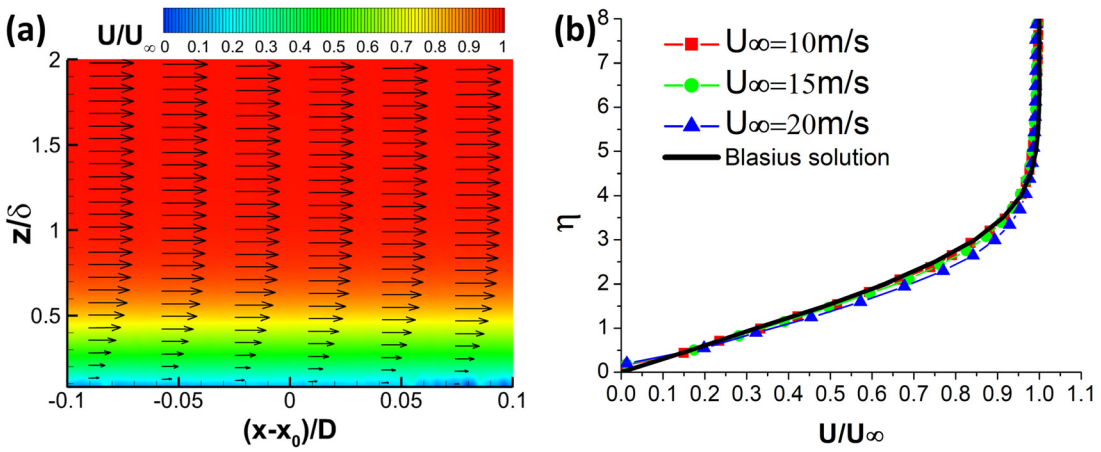

FIG. 2. PIV measurement results of the boundary layer airflow over the test plate. (a) PIV measurement results with $U_\infty = 20$ m/s (x_0 denotes the center of the test plate; δ is the boundary layer thickness with its speed being 0.99 U_∞). (b) Measured velocity profiles at the center of the test plate (i.e., at $x = x_0$) (η denotes the normalized vertical position for the Blasius equation).

grid images (i.e., the distorted images with the wind-driven water film/rivulet flow on the test plate) were acquired for each test case. A cross-correlation algorithm[32] was used to determine the displacement maps of the projected grids in the distorted images against their original positions in the reference images. With the displacement-to-thickness conversion ratio map determined via a calibration procedure similar to that described in Zhang *et al.*,[30] the film thickness distribution of the water film/rivulet flow over the test plate was determined quantitatively based on the displacement maps obtained from cross-correlation-based DIP image processing. With the same DIP system as the one used in the present study, Zhang *et al.*[30] measured the 3D shape of a spherical cap with known dimensions for the DIP measurement validation. The uncertainty level of the DIP measurements was found to be about 0.02 mm, which is about 0.5% of the nominal height of $H = 4.00$ mm. Further information about the technical basis of the DIP technique and its applications to quantify wind-driven surface water flows pertinent to aircraft icing phenomena can be found in our recently published papers.[12,30,33]

It should be noted that, in order to enhance light reflection over the free surface of the water film/rivulet flow for improved quality of the acquired DIP images (i.e., for a better DIP measurement accuracy), a small amount of flat white latex dye (i.e., ~1.0% in volume fraction) was premixed with the water in the reservoir. After adding the latex dye into the water, while the viscosity of the working liquid was found to be almost unchanged (i.e., ±2% in variation), its surface tension was found to be reduced from $\sigma \approx 0.072$ to $\sigma \approx 0.042$ N/m. The advancing contact angle of liquid droplets over a tilted test plate was measured by using a shadowgraph-based imaging technique, which was found to be $\theta_a \approx 80°$.

III. EXPERIMENTAL RESULTS AND DISCUSSION

A. Transient runback behaviors of the wind-driven film/rivulet flows

After being carefully calibrated and validated, the DIP system was utilized to characterize the wind-driven water film/rivulet flows over the flat test plate under different test conditions. Figure 3 shows some typical DIP measurement results to reveal the transient behaviors of the wind-driven film/rivulet flows in terms of the measured film thickness distributions over the test plate. During the experiments, the freestream speed of the incoming airflow was changed from $U_\infty = 5$ to $U_\infty = 20$ m/s. While very similar water runback characteristics were also observed for the test cases with a higher water flow rate $Q = 200$ ml/min, only the measurement results for the test case with $Q = 100$ ml/min are shown here for conciseness.

As revealed clearly in Fig. 3(a), after turning on the pump to inject water flowing over the test plate at a time $t = 0$, a rather uniform water film flow was found to be generated over the test plate for the test case with relatively low airflow velocity (i.e., the freestream wind speed $U_\infty = 5$ m/s). While the free surface of the wind-driven film flow was found to be rather flat with the averaged film thickness near the film front being about 2.2 mm (i.e., $H_{ave} \approx 2.2$ mm), no obvious surface waves were observed at the water/air interface. The wind-driven film flow was found to have a rather straight front contact line, which was moving slowly (i.e., having an averaged runback velocity of $\overline{V}_{\text{runback}} \approx 4.5$ mm/s, which was estimated based on the time needed for the film/rivulet front to flow over the measurement window) as driven by the boundary layer airflow with $U_\infty = 5$ m/s.

As the freestream velocity of the airflow was increased to $U_\infty = 10$ m/s, while the averaged film thickness of the wind-driven water film flow near the film front was found to be reduced to about 1.5 mm (i.e., $H_{ave} \approx 1.5$ mm), well-organized surface waves were found to be generated at the air/water interface for this test case, as shown clearly in Fig. 3(b). The surface waves were found to be sinusoidal-shaped and have rather uniform shape along the spanwise direction, i.e., having very similar characteristics as the two-dimensional (i.e., 2D) surface waves observed in the experimental study of Liu *et al.*.[27] It was also found that, while the wind-driven water film flow runs back with a much higher averaged moving speed (i.e., the averaged moving velocity of the front contact line was increased to $\overline{V}_{\text{runback}} \approx 30$ mm/s, which is about six times higher than that with $U_\infty = 5$ m/s), the front contact line was found to move forward in a stumbling motion. Instead of advancing smoothly and continuously, the front contact line of the wind-driven film flow was found to stop moving from time to time, coupling well with the propagation of the surface waves generated at the air/water interface. More specifically, the film front/head was found to progress very slowly or to not move at all (i.e., in stagnation) when the film front/head has a relatively uniform film thickness distribution. As the crests of the surface waves approach the film front contact line to cause the formation of a high-rise film front/head, the film front contact line was found to move forward very rapidly (i.e., in acceleration) to a further downstream location. Then, the moving speed of the film front/head was found to slow down again (i.e., in deceleration) until next crests of the surface waves approached the film front/head to make the film front/head run back in a stumbling motion with obvious "acceleration-and-deceleration" cycles. The characteristic period of the acceleration-and-deceleration cycles was found to be 0.227 s, for the test case of $U_\infty = 10$ m/s, which correlated well with the dominant frequency of the 2D surface waves (i.e., $f \approx 4.4$ Hz) generated at the air/water interface of the wind-driven film flow.

As shown clearly in Fig. 3(c), when the incoming airflow velocity was further increased to $U_\infty = 15$ m/s, the wind-driven water film flow over the test plate was found to become much thinner with its film thickness being only about 0.8 mm (i.e., $H \approx 0.8$ mm). Instead of forming well-organized 2D waves, the surface waves generated at the air/water interface were found to be evolved into much more complex three-dimensional (i.e., 3D) wave structures. Due to rapid growth of the 3D surface waves, the front contact line of the wind-driven film flow was found to be deformed significantly along the spanwise direction, and two rivulet flows, which have much faster moving speeds at the rivulet heads, were found to be generated at the two sides of the wind-driven film flow, as shown clearly in Fig. 3(c). The fast transition of surface waves from 2D waves to more complex 3D waves at relatively high wind speeds (i.e., $U_\infty \geq 15$ m/s) was also reported in the previous studies of Craik[34] and Liu *et al.*[27] Due to the generation of 3D surface waves, the runback motion of the wind-driven water film/rivulet flow was found to become much more unsteady. While the averaged runback speed of the film front/head was found to increase significantly, reaching up to $\overline{V}_{\text{runback}} \approx 100$ mm/s, the "acceleration-and-deceleration" runback feature was found to become more noticeable for this test case. While the film/rivulet heads were found to move forward in a more obvious stumbling motion, the characteristic period of the acceleration-and-deceleration cycles was found to decrease to 0.135 s for this test case, which is much shorter than for the test case with a lower speed of $U_\infty = 10$ m/s.

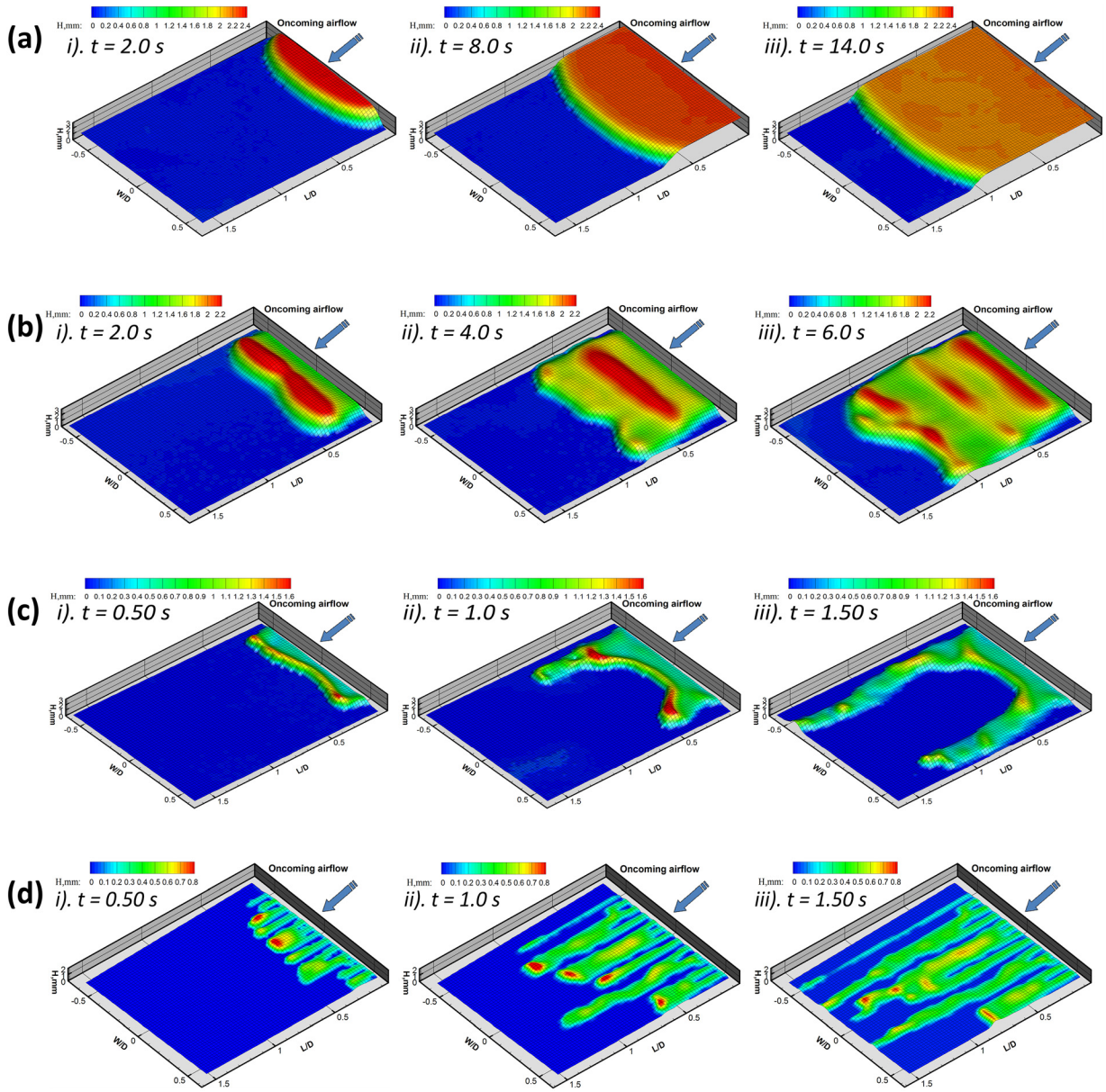

FIG. 3. DIP measurement results to reveal the transient runback process of wind-driven film/rivulet flows under different test conditions. (a) The test case with $U_\infty = 5$ m/s. (b) The test case with $U_\infty = 10$ m/s. (c) The test case with $U_\infty = 15$ m/s. (d) The test case with $U_\infty = 20$ m/s.

The DIP measurement results given in Fig. 3(d) reveal clearly that, as the airflow velocity was further increased to $U_\infty = 20$ m/s, the front contact line of the water film was found to be teared off and broken into multiple segments right after water was injected onto the test plate. As a result, multiple rivulet flows were found to be generated downstream of water injection holes. Corresponding to the much higher airflow velocity for this test case, while the wind-driven film/rivulet flows were found to run back much faster with the averaged runback speed ($\overline{V}_{\text{runback}} \approx 200$ mm/s), the thickness of the film/rivulet flows on the test plate was found to be further decreased to become less than ~0.5 mm(i.e., $H < 0.5$ mm). In contrast, the widths of the rivulets were found to grow gradually as they moved downstream. Some of the rivulets were even found to merge with the neighboring rivulets as they grew wider enough to wet the dry patches between the rivulets. The merging of neighboring rivulets was found to cause obvious meandering of the rivulet heads along their moving paths. While the wind-driven rivulet flows were also observed to run back in stumbling motions, since the runback motions of the wind-driven film/rivulet flows were found to become much more chaotic, no obvious dominant frequencies can be easily identified to represent the

characteristic period of the acceleration-and-deceleration cycles for the wind-driven rivulet flows.

B. Quantification of the runback characteristics of the wind-driven rivulet flows

In order to characterize the stumbling motion of wind-driven water film/rivulet flows as they run back over the test plate more clearly and quantitatively, the DIP measurement results were further processed to extract the moving trajectories of the film fronts or rivulet heads of the film/rivulet flows, thereby, determining the instantaneous runback speed of the wind-driven film/rivulet flows under different test conditions. As shown schematically in Fig. 4, the locations of the front contact lines of the wind-driven water film/rivulet flows were determined based on the instantaneous DIP measurement results with a threshold film thickness value of 0.05 mm (i.e., the red line highlighted in Fig. 4 with the measured film thickness of $H = 0.05$ mm). Then, the utmost downstream location of the front contact line at each frame of the instantaneous DIP measurements was identified, e.g., the points of A and A′ indicated in Figs. 4(a) and 4(b). Finally, the displacement of the utmost positions of the front contact line over the time interval between two successive frames was used to determine the instantaneous runback velocity of the wind-driven film/rivulet flow (i.e., $V = \Delta l/\Delta t$).

Figure 5 gives the results extracted from the DIP measurements to quantify the transient runback behavior of the wind-driven film/rivulet flow for the test case with a freestream wind speed $U_\infty = 5$ m/s and $Q = 100$ ml/min. While Fig. 5(a) shows a typical instantaneous DIP measurement result to reveal the front line of the wind-driven film flow over the test plate, the extracted film thickness profile along the centerline of the wind-driven film flow [i.e., in the plane highlighted in Fig. 5(a)] at different time instants is shown in Fig. 5(b). It can be seen quantitatively that, when the incoming airflow velocity was relatively low (i.e., $U_\infty = 5$ m/s), the free surface of the wind-driven film/rivulet flow was found to be quite flat without forming any obvious surface waves at the air/water interface. Based on the time evolution of the utmost location of the film front given in Fig. 5(c), the wind-driven film/rivulet flow was found to take about 20 s to move through the DIP measurement window (i.e., 80 mm along the flow direction) for this test case. As shown quantitatively from the estimated runback velocity of the film front given in Fig. 5(d), while the wind-driven film flow over the test plate was found to move very slowly (i.e., having an averaged runback speed $\overline{V}_{\text{runback}} \approx 4.0$ mm/s), the instantaneous runback velocity of the film front shown in Fig. 5(d) was found to be always greater than zero (i.e., $V_{runback} > 0$), indicating that the wind-driven film flow would progress continuously (i.e., the runback film front was never in stagnation) for the test case with $U_\infty = 5$ m/s. Based on the measured runback speed data given in Fig. 5(d), the acceleration rate of the moving front contact line of the wind-driven film flow can also be estimated, which was found to be on the order of 10^{-4} m/s^2, indicating that the wind-driven film flow under the test condition of $U_\infty = 5$ m/s could be considered a "quasi-steady" film flow. As described in Hartley and Murgatroyd[20] in developing the minimum film thickness criteria for shear-driven thin film flows, the shear force exerted by the incoming airflow at the air/water interface should be able to surpass the restraining surface tension force under the test conditions of $U_\infty = 5$ m/s and $Q = 100$ ml/min in order to drive the film front moving forward.

Figure 6 gives the DIP measurement results for the test case with the wind speed being increased to $U_\infty = 10$ m/s, while the water flow rate was kept at the same level of $Q = 100$ ml/min. It can be seen clearly that, due to the formation of well-organized surface waves at the air/water interface, the film thickness of the wind-driven film flow was found to vary significantly along the flow direction, as revealed clearly in Fig. 6(b). Corresponding to the higher incoming wind speed for this case, the wind-driven film/rivulet flow was found to move much faster in comparison to the test case with a lower incoming wind speed of $U_\infty = 5$ m/s. More specifically, the averaged runback velocity of the film/rivulet flow driven by the boundary layer airflow with $U_\infty = 10$ m/s was found to increase to $\overline{V}_{ave.} \approx 14$ mm/s, which is about 3.5 times higher than that of the case with $U_\infty = 5$ m/s. As revealed clearly by moving trajectories of the front contact line in the middle plane of the wind-driven film/rivulet flow given in Fig. 6(c), the film front was found to stop moving from time to time, resulting in the formation of multiple flat plateaus in the film front moving trajectories for this test case. Since the film front was in stagnation from time to time, the instantaneous runback velocity of the film front was found to become zero frequently, as shown clearly in Fig. 6(d). As a result, the wind-driven water film flow was found to move forward in a stumbling runback motion with obvious "acceleration-and-deceleration" cycles, as described above. In summary, the runback characteristics of the wind-driven film flow for this test case was found to become very different from those with a lower wind speed of

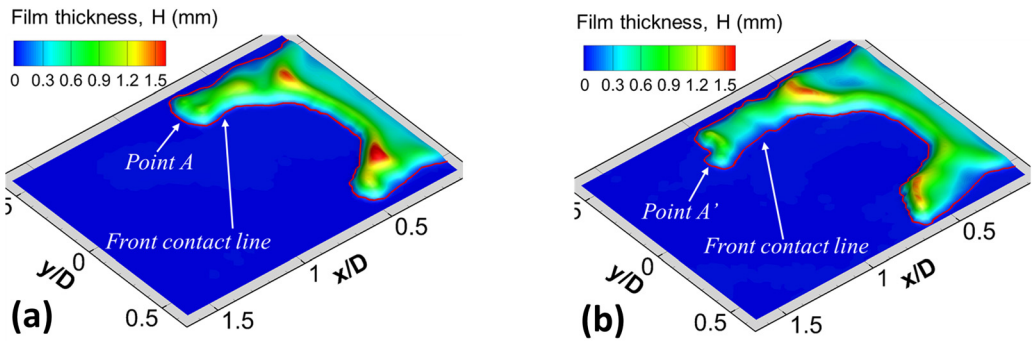

FIG. 4. Determination of the instantaneous runback speed of the rivulet head based on two successive frames of the instantaneous DIP measurements. (a) Measured film thickness at time $t = t_0$. (b). Measured film thickness at time $t = t_0 + \Delta t$.

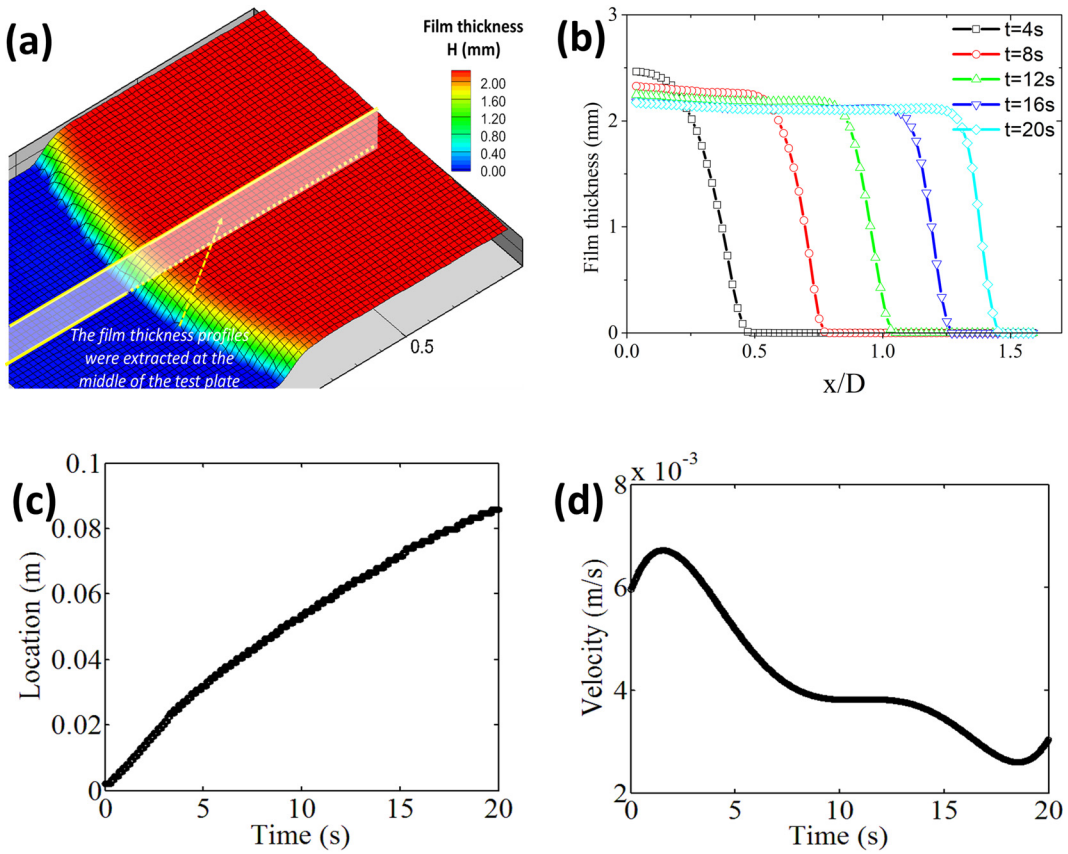

FIG. 5. Time evolutions of the front contact line location and runback velocity of the wind-driven film/rivulet flow for the test case with $U_\infty = 5$ m/s and Q = 100 ml/min. (a) An instantaneous DIP measurement result. (b) Extracted water film thickness profiles. (c) Location of the front contact line. (d) Runback velocity of the film/rivulet flow.

$U_\infty = 5$ m/s. Corresponding to the formation of surface waves at the air/water interface, the wind-driven film flow was found to run back over the test plate in an obvious stumbling runback motion with the film front moving forward in acceleration-and-deceleration cycles.

Figure 7 shows the DIP measurements under the test condition with a wind speed of $U_\infty = 15$ m/s and water flow rate of $Q = 200$ ml/min. Due to a stronger aerodynamic shear force exerted by the airflow with higher speed, the front contact of the film flow was found to break down rapidly as water was injected on the test plate, causing the formation of multiple rivulets over the test plate, as shown clearly in Fig. 7(a). As revealed clearly by the measured film thickness profile extracted along the center of rivulet #2, while the wind-driven film/rivulet flow was found to become much thinner (i.e., the averaged film thickness becoming less than 0.7 mm), irregular surface waves (i.e., 3D surface waves) were found to be generated at the air/water interface to induce much more complicated film thickness distributions for the wind-driven film/rivulet flow. For the three rivulet flows formed on the test plate, even though they were driven by the same incoming airflow of $U_\infty = 15$ m/s, the rivulet head with narrower rivulet width (e.g., rivulet #3) was found to move much faster than those with greater rivulet width (i.e., rivulet #1 and #2). As shown clearly in Fig. 7(d), corresponding to the formation of complicated 3D surface waves at the air/water interface, the moving speeds of the rivulet heads were found to fluctuate significantly with the instantaneous runback speeds, even becoming zero sometimes for all the three rivulet flows. As described above, the fluctuating frequency revealed in the time evolution profiles of the instantaneous rivulet heads' runback speed (i.e., the frequency of the acceleration-and-deceleration runback cycles) was also found to increase monotonically as the wind speed increases. It should also be noted that, while the DIP measurement results for the test case with the airflow speed being further increased to $U_\infty = 20$ m/s also reveal very similar runback characteristics for the wind-driven film/rivulet flow, the measurement data are not presented here for conciseness. In summary, the DIP measurement results reveal clearly that, as the incoming wind speed increases, while more complex 3D surface waves were found to be generated at the air/water interface, the wind-driven film flow became highly unsteady with the front contact line breakoff rapidly to form multiple isolated rivulet flows. As driven by the airflow over the test plate, the rivulet flows were found to be meandering and merging with the neighboring rivulets with the rivulet heads moving forward in stumbling motion with obvious "acceleration-and-deceleration" cycles.

Figure 8 gives the instantaneous DIP measurement results near a moving rivulet head at three selected instants, which can be used to clearly reveal the coupling of the surface waves generated at the air/water interface with a stumbling runback motion of the wind-driven

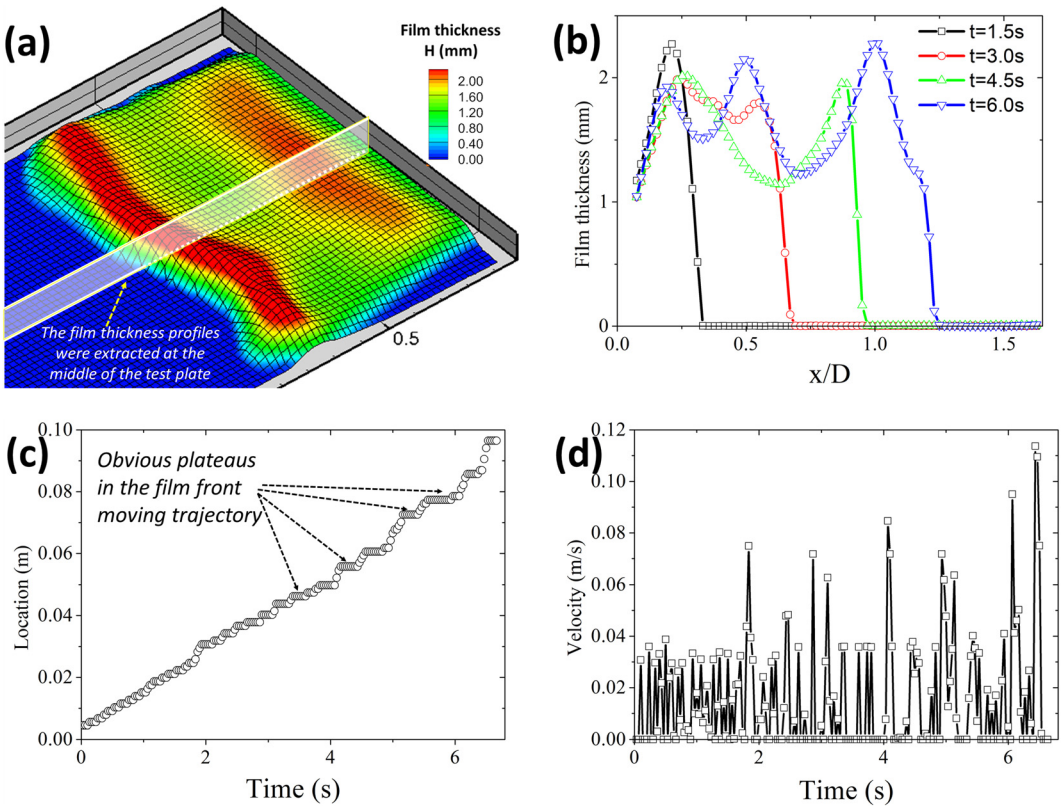

FIG. 6. Time evolutions of the front contact line location and runback velocity of the wind-driven film/rivulet flow for the test case with $U_\infty = 10$ m/s and Q = 100 ml/min. (a) An instantaneous DIP measurement result. (b) Extracted water film thickness profiles. (c) Location of the front contact line. (d) Runback velocity of the film/rivulet flow.

flow/rivulet flows. While Fig. 8(a) gives the measured runback speed of the rivulet head under the test conditions of $U_\infty = 10\,\mathrm{m/s}$ and $Q = 200\,\mathrm{ml/min}$, Figs. 8(b)–8(d) show the "zoom-in" view of the film thickness distributions near the rivulet head at three selected moments (i.e., right before and after the rivulet head was in stagnation). It is well known that, for a wind-driven film/rivulet flow, the summation of the aerodynamic drag force acting on the rivulet head (i.e., mainly form drag) and the aerodynamic shear force (i.e., skin friction force) at the air/water interface should be greater than the restraining force due to surface tension in order to drive the film/rivulet flow moving forward. As shown clearly in Fig. 8(b), at time $t = t_1$ (i.e., right before the rivulet head was in stagnation), while a crest of the surface wave was moving toward the rivulet front, the rivulet flow was found to have a low-rise rivulet head with its film thickness being smaller than that at the rivulet body. Since the aerodynamic drag force acting on the low-rise rivulet head would be relatively small, the formation of such a low-rise rivulet head is not favorable to generate enough aerodynamic drag force to overcome the restraining surface tension force. As a result, the rivulet head was found to be in a decelerated runback motion at the instant $t = t_1$ (i.e., the moving speed of the rivulet head becoming smaller and smaller), as shown clearly in Fig. 8(a).

The DIP measurement result given in Fig. 8(c) reveals clearly that, while the rivulet head was in stagnation (i.e., the runback speed being zero), the crest of the surface waves arrived at the rivulet front at the instant $t = t_2$. As a result, the film thickness at the rivulet head was found to be increased substantially, causing the formation of a high-rise hump at the rivulet head with its film thickness becoming much greater than that at the rivulet body. Corresponding to the formation of a high-rise hump-shaped rivulet head, the aerodynamic drag force acting on the rivulet head would become much greater, in comparison to the case with a low-rise rivulet head shown in Fig. 8(b). The rapidly increased aerodynamic drag force acting on the rivulet head would be very favorable to surpass the restraining surface tension force to push the rivulet head moving forward. Therefore, the runback of the wind-driven rivulet flow was found to be accelerated after time $t = t_2$, as shown clearly by the runback velocity data given in Fig. 8(a).

As the rivulet front reached a further downstream location at the instant $t = t_3$, since the rivulet head was found to become relatively flat again as shown clearly in Fig. 8(d), the corresponding aerodynamic drag force acting on the rivulet head would become much smaller again, resulting in the deceleration of the runback motion for the wind-driven film/rivulet flow. This would lead to a new deceleration-and-acceleration cycle for the rivulet head of the wind-driven rivulet/film flow to run back over the test plate. In summary, the DIP measurement results given in Fig. 8 reveal clearly that, by changing the local film thickness distributions near the rivulet head dynamically, the surface waves generated at the water/air interface would induce significant variations of the aerodynamic drag force acting on the

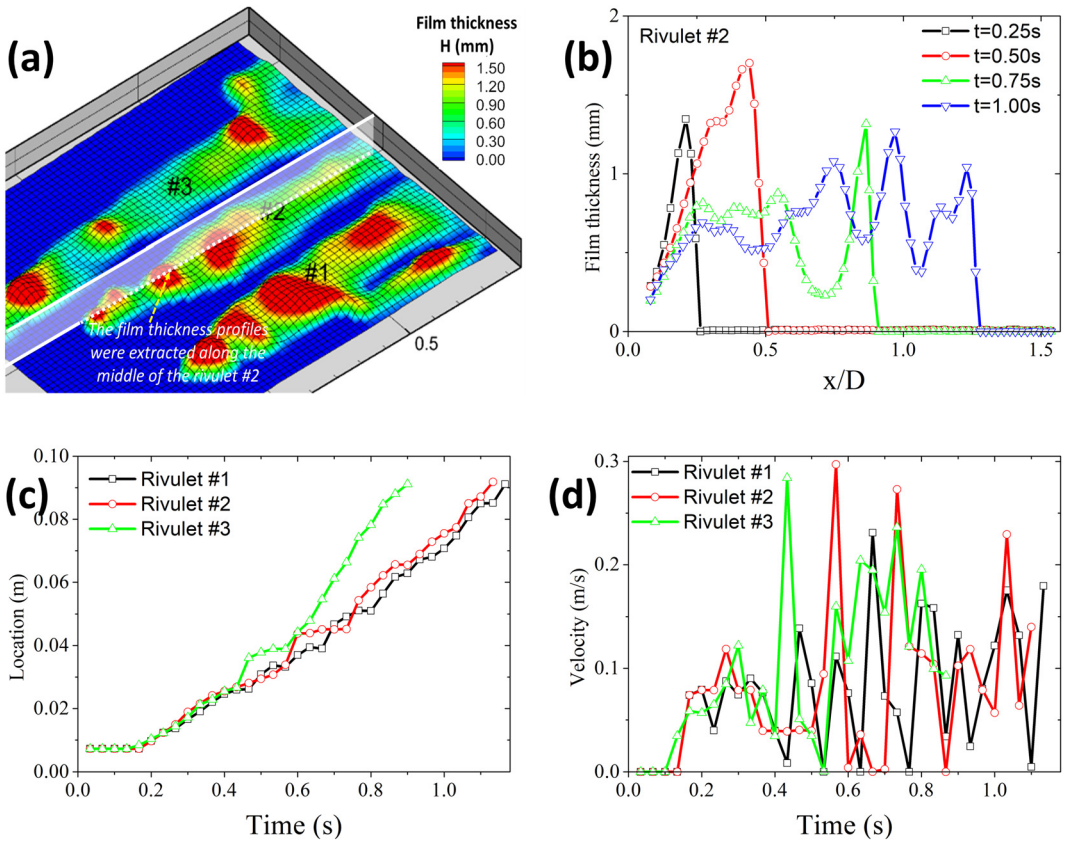

FIG. 7. Time evolutions of the front contact line location and runback velocity of the wind-driven film/rivulet flow for the test case with $U_\infty = 15$ m/s and Q = 200 ml/min. (a) An instantaneous DIP measurement result. (b) Extracted water film thickness profiles. (c) Location of the front contact line. (d) Runback velocity of the film/rivulet flow.

rivulet head. As a result, the wind-driven film/rivulet flow was found to run back in a stumbling motion with the rivulet head moving forward in obvious deceleration-and-acceleration cycles.

IV. FORCE BALANCE ANALYSIS OF THE WIND-DRIVEN FILM/RIVULET FLOWS

The DIP measurement results given above reveal clearly that, as the surface waves were found to be generated at the air/water interface at relatively high incoming wind speeds (e.g., $U_\infty \geq 10$ m/s), the wind-driven water film/rivulet flows would run back in a stumbling motion with the film/rivulet heads moving forward in deceleration-and-acceleration cycles. By leveraging the quantitative DIP measurement results, a comprehensive force balance (FB) analysis is performed in the present study in order to gain further insight into the underlying physics pertinent to the stumbling runback motion of wind-driven water film/rivulet flows.

It should be noted that Hartley and Murgatroyd[20] developed a FB criterion to predict the dry-patch rewetting process for thin film flows driven by surface shear. The breakoff of the stagnated rivulet head to re-start the runback process for a wind-driven rivulet/film flow investigated in the present study is very similar to the dry-patch rewetting process studied by Hartley and Murgatroyd.[20] Therefore, a similar methodology was adopted in the present study for the FB analysis of wind-driven film/rivulet flows.

As revealed clearly in Fig. 8(c), while the rivulet head of a wind-driven film/rivulet flow was in stagnation, due to the arrival of crest of surface waves at the rivulet front, a high-rise hump would be formed at the rivulet head with its film thickness becoming noticeably greater than that at the rivulet body. Therefore, at the moment when the rivulet head was in stagnation, the wind-driven film/rivulet flow was simplified to having a high-rise hump-shaped rivulet head and relatively flat rivulet body, as shown schematically in Fig. 9.

It should also be noted that, for the dry-patch rewetting process studied by Hartley and Murgatroyd,[20] only two relevant forces were considered in the FB analysis: the excess pressure force built inside the film head and the restraining force due to surface tension. Hartley and Murgatroyd[20] suggested that the dry patch would be re-wetted when the excess pressure force surpasses the restraining surface tension force. More recently, McAlister *et al.*[28] conducted an FB analysis to model the breakoff of wind-driven rivulet/droplet flows in microgravity and terrestrial-gravity conditions. While an empirical model was suggested to estimate the aerodynamic drag forces acting on rivulets/droplets, the excess pressure force built inside the rivulet heads was not considered in the FB analysis of McAlister *et al.*[28] In the present study, a comprehensive FB analysis is performed to examine all the relevant forces in order to elucidate the underlying physics pertinent

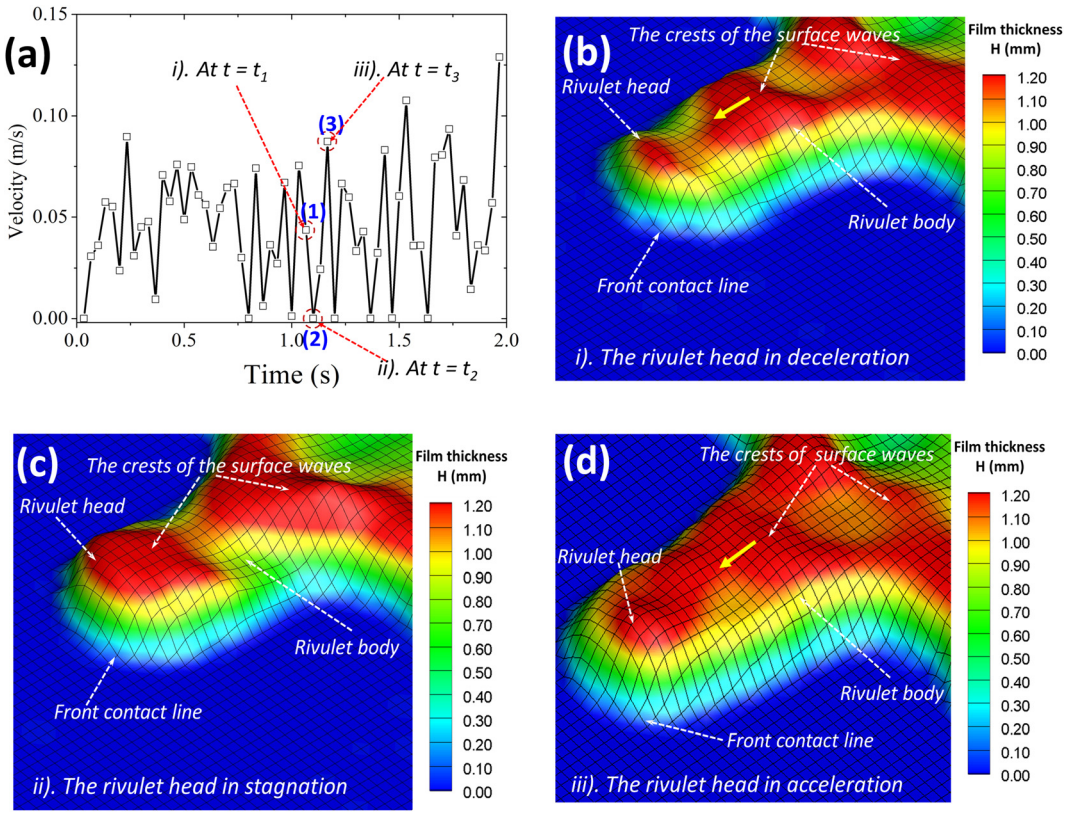

FIG. 8. DIP measurement results to reveal the effect of surface waves on the runback process of wind-driven water film/rivulet flow over the test plate. (a) Runback velocity of the rivulet front. (b) The DIP measurement result at $t = t_1$. (c) The DIP measurement result at $t = t_2$. (d) The DIP measurement result at $t = t_3$.

to the breakoff of the stagnated rivulet head to re-start the runback motion for the wind-driven rivulet/film flow.

For the wind-driven film/rivulet flows investigated in the present study, three different forces were believed to play very important roles in determining the runback characteristics of the film/rivulet head as revealed from the DIP measurement results given schematically in Fig. 9, which includes the excess pressure force built inside the rivulet head of a wind-driven film/rivulet flow, F_P; aerodynamic drag force (i.e., form drag) acting on the rivulet head exerted by the incoming air-flow, F_D; and the restraining force due to surface tension along the front contact lines, F_σ. Since the rivulet head was assumed to be in stagnation, the front contact line of the wind-driven film/rivulet flow would not be able to move forward until the summation of the aerodynamic drag force acting on the rivulet head and the excess pressure force built inside the rivulet head becomes greater than the restraining surface tension force, which can be expressed as follows

$$F_P + F_D \geq F_\sigma. \tag{1}$$

A. Estimation of the restraining force due to surface tension

As described in the FB analysis of Hartley and Murgatroyd[20] and McAlister *et al.*,[28] the restraining force due to surface tension at the rivulet head can be estimated as

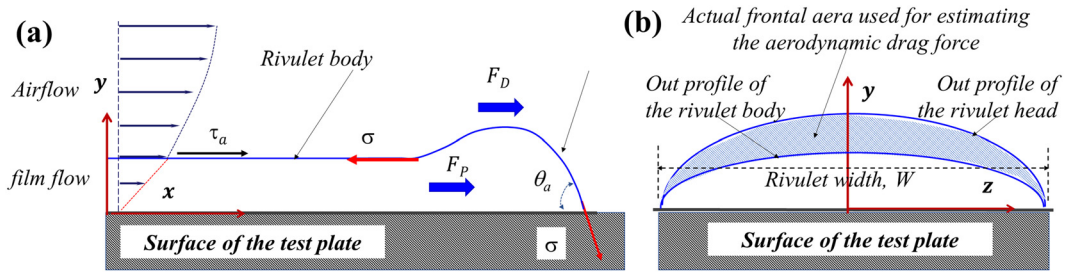

FIG. 9. Schematics used for FB analysis with a rivulet head in stagnation (sketch not in scale): (a) side view and (b) end view.

$$F_\sigma = L\sigma(\cos\theta_r - \cos\theta_a), \tag{2}$$

where L is the contact line length at the rivulet head; θ_r and θ_a denote the receding and advancing contact angles of the film/rivulet contact line, respectively; and σ is surface tension coefficient.

As revealed clearly by the DIP measurement results given above, the characteristic lengths of the rivulet heads for the wind-driven film/rivulet flows on the test plate of the present study (i.e., rivulet width and length) are usually much larger than the film thickness. Therefore, as shown schematically in Fig. 9, the receding contact angle of the contact line at the back of the rivulet head would approach zero, making $\cos(\theta_r) \approx 1.0$. Meanwhile, while the hump-shaped rivulet head is three-dimensional in shape, since the rivulet head usually has a very large width-to-height ratio (i.e., $W/H > 5$ as revealed from the DIP measurement results given in Fig. 8(c), where W and H are the width and height of the rivulet head, respectively), the estimation of the restraining force due to surface tension can be simplified from a 3D problem to a 2D problem. Therefore, the restraining forces due to surface tension at the rivulet head can be approximated as

$$F_\sigma = W\sigma(1 - \cos\theta_a). \tag{3}$$

As described above, $\sigma = 0.04\,\mathrm{N/m}$ for the working liquid used in the present study (i.e., water pre-mixed with 1.0% latex dye). The advancing contact angle at the front contact line of the wind-driven film/rivulet flows was measured to be $\theta_a \approx 80°$. Therefore, the restraining surface tension force at the rivulet head would be almost independent of the incoming wind speed and water flow rate of the wind-driven film/rivulet flows over the test plate.

B. Estimation of the excess pressure force built inside the rivulet head

Similar to the description of Hartley and Murgatroyd,[20] as the rivulet head was in stagnation (i.e., the runback speed becoming zero), the liquid fluid in a stream tube inside a surface shear-driven film flow with an incoming flow velocity u_w would reduce gradually to zero at the rivulet head, resulting in an excess pressure built inside the film/rivulet head, which can be expressed as

$$\Delta p = 0.5\rho_w u_w^2. \tag{4}$$

Therefore, the total excess pressure force built inside the rivulet head can be estimated by integrating the excess pressure across the entire film flow field, and can be express as

$$F_P = \int_0^W \int_0^H 0.5\rho_w u_w^2 . dydz, \tag{5}$$

where ρ_w is the liquid density, which is 1.0 g/ml for the water used in the present study.

As described above, since the wind-driven film/rivulet flows investigated in the present study usually have a very large width-to-height ratio (i.e., $W/H > 5$), they can be approximated as two-dimensional flows. As described in Al-Khalil *et al.*,[26] the velocity distribution within a rivulet section can be determined by solving the Laplace equation as follows:

$$\frac{\partial^2 u_w}{\partial y^2} + \frac{\partial^2 u_w}{\partial z^2} = 0, \tag{6a}$$

$$u_w|_{y=0} = 0, \tag{6b}$$

$$\left.\frac{\partial u_w}{\partial z}\right|_{z=0} = 0, \tag{6c}$$

$$\mu_w \frac{\partial u_w}{\partial r} = \tau_a. \tag{6d}$$

Equation (6b) is the no-slip condition at the water–solid interface, Eq. (6c) assumes the velocity profile is symmetric along the spanwise direction in relation to the rivulet centerline. Equation (6d) indicates the shear stress, τ_a, at the air/water interface is continuous, where r is the radial direction (i.e., normal to the local water–air interface). The shear stress at the air/water interface is assumed to be a constant over the rivulet surface and can be estimated based on the Blasius solution of $\tau_a = 0.664/\sqrt{Re_x}$ for different test conditions. μ_w in Eq. (6d) is the viscosity of water. Al-Khalil *et al.*[26] solved the above equations numerically, and found that, as the width-to-height ratio of the film flow became greater than five (i.e., $W/H > 5$), the velocity distribution inside the rivulet flow would be simplified by using a linear velocity profile of

$$u_w = \tau_a y/\mu_w. \tag{7}$$

Therefore, the excess pressure force built inside the rivulet head could be expressed as

$$F_P = \int_0^W \int_0^H 0.5\rho_w u_w^2 . dydz = W\int_0^H 0.5\rho_w(\tau_a y/\mu_w)^2 dy = \frac{\rho_w \tau_a^2 H^3 W}{6\mu_w^2}. \tag{8}$$

As shown clearly in Eq. (8), the excess pressure head built inside the rivulet head of the wind-driven film/rivulet flow would increase quadratically with the increasing aerodynamic shear stress acting on the air/water interface as expected. It should also be noted that the excess pressure head built inside the rivulet head would increase cubically with the film thickness, indicating that a thicker film flow would be more favorable in generating enough excess pressure force at the film/rivulet head to surpass the restraining surface tension force in order to enable the film/rivulet front to move forward.

C. Estimation of the aerodynamic drag force acting on the film/rivulet head

An empirical model was suggested by McAlister *et al.*[28] for analyzing the aerodynamic forces acting on the rivulet heads of wind-driven rivulet/droplet flows under microgravity and terrestrial-gravity conditions. While very similar hump-shaped rivulet heads were also observed by McAlister *et al.*,[28] the rivulet heads were simplified as semi-ellipsoids with semi-axis height, H (i.e., the maximum water depth); semi-minor axis length, b (i.e., the rivulet width); and semi-major axis, a (i.e., the rivulet length) of the elliptical area on the test plate. McAlister *et al.*[28] suggested that the aerodynamic drag force acting on a rivulet head can be estimated as

$$F_D = C_D \frac{1}{2}\rho_a U_\infty^2 \cdot A_{frontal}, \tag{9}$$

where C_D is the drag coefficient of the hump-shaped rivulet head; $A_{frontal}$ is the projected frontal aera of the rivulet head exposed to the airflow. After performing a comprehensive numerical study to characterize the airflows over semi-ellipsoids with different aspect ratios,

McAlister *et al.*[28] suggested that the C_D value would be about 0.6 (i.e., $C_D \approx 0.6$) for hump-shaped rivulet heads.

In the present study, the empirical model suggested by McAlister *et al.*[28] was adopted to estimate the aerodynamic drag forces acting on the hump-shaped rivulet heads of the wind-driven film/rivulet flows. It should be noted that, for the wind-driven rivulets/droplets studied by McAlister *et al.*,[28] the rivulet flows had very big rivulet heads with much narrower rivulet bodies or the rivulet heads were found to be completely separated from their bodies to become isolated droplets. Therefore, McAlister *et al.*[28] suggested that projected frontal aera of the rivulet head exposed to the airflow could be estimated by the projected area of the semi-ellipsoid in the airflow direction, i.e., $A_{frontal} \approx \frac{\pi}{2} bH$. However, due to a much larger wetted aera for wind-driven film/rivulet flows over the test plate pertinent to aircraft icing phenomena, the wind-driven film/rivulet flows investigated in this study were found to have relatively small rivulet heads and more significant rivulet bodies, as revealed clearly by the DIP measurement results given in Fig. 8. Therefore, the actual frontal area of the hump-shaped rivulet head exposed to the incoming airflow would be the projected area of the rivulet head subtracting that of the rivulet body (i.e., $A_{frontal} = A_{head} - A_{body}$), which is indicated by the shaded area given in Fig. 9(b). Furthermore, since the rivulet head usually has a very large width-to-height ratio (i.e., $W/H > 5$ as revealed by the DIP measurement results), the projected frontal area of the rivulet head exposed to the incoming airflow can be further simplified as

$$A_{frontal} = A_{head} - A_{body} = W\left(\overline{H_{rh}} - \overline{H_{rb}}\right), \tag{10}$$

where W is the rivulet width. $\overline{H_{rh}}$ and $\overline{H_{rb}}$ are the average film thicknesses at the rivulet head and rivulet body, which can be determined based on the DIP measurement results near the rivulet head, similar to those shown in Fig. 8.

D. FB criteria for the breakoff of a stagnated rivulet head to re-start the runback process

As expressed in Eq. (1), a stagnated rivulet head would re-start the runback process if the summation of the aerodynamic drag force acting on the film/rivulet head and the excess pressure force built inside the rivulet head becomes greater than the restraining force due to the surface tension. By substituting Eqs. (3), (8), and (9) intoEq. (1), the FB criteria for the breakoff of a stagnated rivulet head to re-start the runback process can be expressed as

$$\frac{\rho_w \tau_a^2 H^3}{6\mu_w^2} + \frac{1}{2} C_d \rho_a U_\infty^2 \left(\overline{H_{rh}} - \overline{H_{rb}}\right) \geq \sigma(1 - \cos\theta_a). \tag{11}$$

It should be noted that, for the test cases with relatively low incoming airflow speed (e.g., the test case with $U_\infty = 5\,\mathrm{m/s}$), since the film front of the wind-driven film/rivulet flow was found to be quite flat with almost the same film thickness at the film head and the body of the film flow, the term $(\overline{H_{rh}} - \overline{H_{rb}})$ in Eq. (11) would become zero. Therefore, the aerodynamic drag force acting on the film font/head would become zero. As a result, the excess pressure force built inside the film front of the wind-driven film flow would need to become greater than the restraining surface tension force in order to push the front contact line of the wind-driven film/rivulet flow to move forward. Therefore, based on the FB criteria given in Eq. (11), the minimum film thickness of the wind-driven film flow should satisfy the following condition:

$$H_{critic} \geq \left[6\sigma(1 - \cos\theta_a)/\rho_w\right]^{\frac{1}{3}} (\mu_w/\tau_a)^{\frac{2}{3}} \approx 1.82\left[\sigma(1 - \cos\theta_a)/\rho_w\right]^{\frac{1}{3}} (\mu_w/\tau_a)^{\frac{2}{3}}, \tag{12}$$

which is exactly the expression suggested by Hartley and Murgatroyd[20] in predicting the minimum film thickness for a surface shear-driven film flow to re-wetting the dry patches.

More specifically, for the test case under the test conditions of $U_\infty = 5\,\mathrm{m/s}$ and $Q = 100\,\mathrm{ml/min}$ (i.e., the test case shown in Fig. 5), while the advancing angle at the front contact line of the wind-driven film flow was found to be about 80° (i.e., $\theta_a \approx 80°$), the surface tension coefficient of the working fluid is $\sigma = 0.04\,\mathrm{N/m}$. The aerodynamic shear stress at the air/water interface can be estimated based on the Blasius solution of $\tau_a = 0.664/\sqrt{Re_x}$. Re_x was estimated to be about 200 000 (i.e., $Re_x \approx 200\,000$) at the center of the test plate based on the relationship $\delta = 5.0x/\sqrt{Re_x}$, where the boundary layer thickness δ was determined based on the PIV measurement results given in Fig. 2. Therefore, the minimum film thickness predicted by using the formula given in Eq. (12) was found to be about 1.84 mm (i.e., $H_{critic} \approx 1.84\,\mathrm{mm}$). As revealed clearly by the DIP measurement results given in Fig. 5(b), the measured film thickness of the wind-driven film flow over the test plate was found to be greater than 2.1 mm (i.e., $H > 2.1\,\mathrm{mm}$). It confirms that the wind-driven film flow over the test plate is indeed thicker than the required minimum film thickness predicted by the FB analysis criteria given in Eq. (12).

As revealed clearly by the DIP measurements given above, as the incoming airflow speed became high enough (e.g., $U_\infty \geq 10\,\mathrm{m/s}$), well-organized 2D or more complicated 3D surface waves were found to be generated at the air/water interface of the wind-driven film/rivulet flows, The formation of surface waves would affect the film thickness distributions near the rivulet/heads significantly. As shown clearly in Fig. 8, as the crests of the surface waves arrived at the film/rivulet head of a wind-driven film/rivulet flow, high-rise humps would be formed at the rivulet heads (i.e., the value of $(\overline{H_{rh}} - \overline{H_{rb}})$ would increase substantially), which would result in a rapid increase in the aerodynamic drag forces acting on the high-rise rivulet heads.

In order to reveal the importance of the three relevant forces to the breakoff of the stagnated rivulet head to re-start the runback process more clearly and quantitatively, the DIP measurement results obtained under different test conditions were used to estimate the three relevant forces described above. Table I summarizes the test conditions used for the FB analysis and the estimated restraining surface tension force f_σ, excess pressure force f_P, and the aerodynamic drag force f_d acting on the stagnated rivulet head per unit span of the wind-driven film/rivulet flow.

As revealed clearly from the estimated force data listed in Table I, corresponding to the formation of much thinner wind-driven film/rivulet flows over the test plate at higher incoming wind speeds, the excess pressure force built inside the film/rivulet head was found to be much smaller in comparison to the other two forces (i.e., being less than 20% of the restraining surface tension force) for all the investigated cases. On the other hand, the aerodynamic drag force acting on the hump-shaped rivulet head was found to play a dominant role in overcoming the restraining surface tension force for the breakoff of the stagnated film/rivulet head to re-start the runback process. More specifically, since the aerodynamic drag force acting on the high-rise film/rivulet head was found to be much greater than the restraining surface tension force, the stagnated film/rivulet heads would be pushed

TABLE I. Comparison of the restraining surface tension force, excess pressure force, and the aerodynamic drag force acting on stagnated rivulet heads under different test conditions.

Cases	$\overline{H_{rh}}$ (mm)	$\overline{H_{rb}}$ (mm)	f_σ (N/m)	f_P (N/m)	f_D (N/m)
$U_\infty = 10\,\mathrm{m/s},\ Q = 100\,\mathrm{ml/min}$	2.71	1.34	0.033	0.003	0.049
$U_\infty = 10\,\mathrm{m/s},\ Q = 200\,\mathrm{ml/min}$	2.72	1.63	0.033	0.006	0.039
$U_\infty = 15\,\mathrm{m/s},\ Q = 100\,\mathrm{ml/min}$	1.63	0.66	0.033	0.001	0.079
$U_\infty = 15\,\mathrm{m/s},\ Q = 200\,\mathrm{ml/min}$	1.51	0.77	0.033	0.002	0.060
$U_\infty = 20\,\mathrm{m/s},\ Q = 100\,\mathrm{ml/min}$	1.02	0.49	0.033	0.001	0.068
$U_\infty = 20\,\mathrm{m/s},\ Q = 200\,\mathrm{ml/min}$	0.85	0.38	0.033	0.0006	0.077

to move forward abruptly, resulting in a rapid increase in the runback velocity of the film/rivulet heads (i.e., the acceleration in the runback process), which is similar to those revealed from the instant $t = t_2$ to the instant $t = t_3$ shown in Fig. 8.

Right after the breakoff of the stagnated rivulet head to re-start the runback process, the film thickness at the film/rivulet head was found to decrease substantially as revealed clearly by the DIP measurement results given in Fig. 8(d). Therefore, a relatively flat, low-rise rivulet head would be formed as the film/rivulet head moved to a further downstream location, resulting in a much smaller aerodynamic force acting on the low-rise film/rivulet head. However, as expressed in Eq. (3), since the restraining surface tension force is only a function of the advancing contact angle of the front contact, which is almost independent of the incoming wind speed and the water flow rate, the restraining surface tension force was found to stay almost unchanged during the runback process. Since the much smaller aerodynamic force acting on the low-rise film/rivulet head could not overcome the restraining surface tension force, the runback speed of the rivulet head would decrease rapidly with the runback process for the wind-driven film/rivulet flow in deceleration until the next crest of the surface waves arriving at the rivulet front to form a new high-rise rivulet head again (i.e., the process revealed from the instant $t = t_1$ to the instant $t = t_2$ given in Fig. 8).

V. CONCLUSIONS

An experimental study was conducted to examine the dynamic runback characteristics of wind-driven water film/rivulet flows over a flat test plate in order to elucidate the underlying physics of the surface water transportation process pertinent to aircraft icing phenomena. The experimental study was conducted in an open-circuit wind tunnel to generate boundary layer airflows with different freestream wind speeds to drive thin water film flows over a flat test plate. During the experiments, a digital image projection (DIP) system was used to achieve non-intrusive, whole-field measurements of the film thickness distributions over the test plate to quantify the transient runback behavior of the wind-driven water film/rivulet flows under different testing conditions.

It was revealed clearly that, as the wind speed over the test plate is relatively low (i.e., $U_\infty < 10\,\mathrm{m/s}$), the wind-driven water film flow was found to be rather steady with a uniform film thickness distribution over the test plate. The film front was found to move forward slowly, but continuously, and no obvious surface waves were found to be generated at the air/water interface. However, as the wind speed became high enough (i.e., $U_\infty \geq 10\,\mathrm{m/s}$), the "steady" runback motion of the wind-driven film flows was found to be interrupted by the presence of surface waves at the air/water interface. The thickness of the water film flow was found to decrease monotonically as the wind speed increases. While the averaged moving speed of the film/rivulet front was observed to increase rapidly with increase in wind speed, the wind-driven film flows were found to run back in a stumbling motion with the film/rivulet heads moving forward in obvious deceleration-stagnation-acceleration cycles. As the wind speed was further increased to higher values (i.e., $U_\infty \geq 15\,\mathrm{m/s}$), while the surface waves generated at the air/water interface were found to transit rapidly from well-organized 2D structures to more complicated 3D structures, the front contact lines of the wind-driven film flows were found to be deformed, stretched, and broken down eventually, resulting in the formation of multiple rivulets to transport the water mass swiftly to further downstream locations in isolated channels. While the water runback process was found to become more and more chaotic, the rivulet heads were found to be meandering along their moving trajectories. The wind-driven rivulet flows were found to become wider as moving downstream results in the merging of neighboring rivulets at further downstream locations.

A comprehensive force balance (FB) analysis was also performed to examine the variations of the relevant forces (i.e., the excess pressure force built inside the film/rivulet head, aerodynamic drag force acting on the film/rivulet head, and the restraining surface tension forces acting along the front contact lines) in order to elucidate the underlying physics pertinent to the changes of the runback characteristics of the wind-driven film/rivulet flows under different test conditions. Simplified formulas were developed to provide quantitative estimations of the relevant forces in order to evaluate their importance in the breakoff of stagnated film/rivulet heads to re-start the runback process. It was revealed clearly that, before the formation of surface waves at the air/water interface (i.e., for the test cases with relatively low incoming wind speed), while the aerodynamic drag force acting on the flat front of the wind-driven film flow was very small, the excess pressure force built inside the film front was found to play a significant role in surpassing the restraining surface tension force in order to push the film flow to move forward. However, for the test cases with relatively high incoming wind speed (i.e., after surface waves were found to be generated at the air/water interface), while the excess pressure forces built inside the film/rivulet heads were found to become much smaller in comparison to other forces, the aerodynamic drag forces acting on the film/rivulet heads were found to play a dominant role in

conquering the restraining surface tension forces to drive the film/rivulet flow running back over the test plate.

ACKNOWLEDGMENTS

This research work is partially supported by the National Science Foundation (NSF) under Award Nos. CMMI-1824840 and CBET-1916380 and Iowa Energy Center for Wind Turbine Icing Study under the IEC Competitive Grant No. 312350.

AUTHOR DECLARATIONS

Conflict of Interest

The authors have no conflicts to disclose.

Authors' Contributions

K.Z. contributed to model design and manufacture, wind tunnel experiments, data acquisition and processing, writing the original draft. H.H. contributed to the development of methodology, formal analysis, writing—review and editing, funding acquisition, and supervision.

DATA AVAILABILITY

The data that support the findings of this study are available from the corresponding author upon reasonable request.

REFERENCES

[1]F. Caliskan and C. Hajiyev, "A review of in-flight detection and identification of aircraft icing and reconfigurable control," Prog. Aerosp. Sci. **60**, 12 (2013).
[2]A. Heinrich, R. Ross, G. Zumwalt, J. Provorse, V. Padmanabhan, J. Thompson, and J. Riley, *Aircraft Icing Handbook* (Gates Learjet Corporation, Wichita, KS, 1991), Vol. 1.
[3]Y. Cao, W. Tan, and Z. Wu, "Aircraft icing: An ongoing threat to aviation safety," Aerosp. Sci. Technol. **75**, 353 (2018).
[4]M. K. Politovich, "Predicting glaze or rime ice growth on airfoils," J. Aircr. **37**, 117–121 (2000).
[5]M. B. Bragg, G. M. Gregorek, and J. D. Lee, "Airfoil aerodynamics in icing conditions," J. Aircr. **23**, 76 (1986).
[6]C. Zhang and H. Liu, "Effect of drop size on the impact thermodynamics for supercooled large droplet in aircraft icing," Phys. Fluids **28**, 062107 (2016).
[7]W. Olsen and E. Walker, "Experimental evidence for modifying the current physical model for ice accretion on aircraft surfaces," Technical Report No. NASA-TM-87184 (NASA Technical Memorandum, 1986).
[8]Y. Liu and H. Hu, "An experimental investigation on the unsteady heat transfer process over an ice accreting airfoil surface," Int. J. Heat Mass Transfer **122**, 707 (2018).
[9]S. P. Otta and A. P. Rothmayer, "Instability of stagnation line icing," Comput. Fluids **38**, 273 (2009).
[10]A. P. Rothmayer and H. Hu, "Solutions for two-dimensional instabilities of ice surfaces uniformly wetted by thin films," AIAA Paper No. AIAA 2012-3133, 2012.
[11]Y. Liu, K. Zhang, W. Tian, and H. Hu, "An experimental investigation on the dynamic ice accretion and unsteady heat transfer over an airfoil surface with embedded initial ice roughness," Int. J. Heat Mass Transfer **146**, 118900 (2020).
[12]Y. Liu, K. Zhang, W. Tian, and H. Hu, "An experimental study to characterize the effects of initial ice roughness on the wind-driven water runback over an airfoil surface," Int. J. Multiphase Flow **126**, 103254 (2020).
[13]R. J. Hansman and S. R. Turnock, "Investigation of surface water behavior during glaze ice accretion," J. Aircr. **26**, 140 (1989).
[14]R. M. Waldman and H. Hu, "High-speed imaging to quantify transient ice accretion process over an airfoil," J. Aircr. **53**(2), 369 (2016).
[15]P. K. Mondal and S. Chaudhry, "Effects of gravity on the thermo-hydrodynamics of moving contact lines," Phys. Fluids **30**, 42109 (2018).
[16]P. K. Mondal, U. Ghosh, A. Bandopadhyay, D. DasGupta, and S. Chakraborty, "Electric-field-driven contact-line dynamics of two immiscible fluids over chemically patterned surfaces in narrow confinements," Phys. Rev. E **88**, 23022 (2013).
[17]P. K. Mondal, D. DasGupta, A. Bandopadhyay, U. Ghosh, and S. Chakraborty, "Contact line dynamics of electroosmotic flows of incompressible binary fluid system with density and viscosity contrasts," Phys. Fluids **27**, 32109 (2015).
[18]D. DasGupta, P. K. Mondal, and S. Chakraborty, "Thermocapillary-actuated contact-line motion of immiscible binary fluids over substrates with patterned wettability in narrow confinement," Phys. Rev. E **90**, 23011 (2014).
[19]G. Kunti, P. K. Mondal, A. Bhattacharya, and S. Chakraborty, "Electrothermally modulated contact line dynamics of a binary fluid in a patterned fluidic environment," Phys. Fluids **30**, 92005 (2018).
[20]D. E. Hartley and W. Murgatroyd, "Criteria for the break-up of thin liquid layers flowing isothermally over solid surfaces," Int. J. Heat Mass Transfer **7**, 1003 (1964).
[21]W. Murgatroyd, "The role of shear and form forces in the stability of a dry patch in two-phase film flow," Int. J. Heat Mass Transfer **8**, 297 (1965).
[22]D. G. Penn, M. L. de Bertodano, P. S. Lykoudis, and S. G. Beus, "Dry patch stability of shear driven liquid films," J. Fluids Eng. **123**, 857 (2001).
[23]M. El-Genk and H. Saber, "Minimum thickness of a flowing down liquid film on a vertical surface," Int. J. Heat Mass Transfer **44**(15), 2809–2825 (2001).
[24]H. H. Saber and M. S. El-Genk, "On the breakup of a thin liquid film subject to interfacial shear," J. Fluid Mech. **500**, 113 (2004).
[25]B. E. Thompson and M. R. Marrochello, "Rivulet formation in surface-water flow on an airfoil in rain," AIAA J. **37**, 45 (1999).
[26]K. M. Al-Khalil, T. G. Keith, Jr., and K. J. De witt, "Development of an anti-icing runback model," AIAA Paper No. AIAA 90-0759, 1990.
[27]Y. Liu, W.-L. Chen, L. J. Bond, and H. Hu, "An experimental study on the characteristics of wind-driven surface water film flows by using a multi-transducer ultrasonic pulse-echo technique," Phys. Fluids **29**, 12102 (2017).
[28]G. McAlister, R. Ettema, and J. S. Marshall, "Wind-driven rivulet breakoff and droplet flows in microgravity and terrestrial-gravity conditions," J. Fluids Eng. **127**, 257 (2005).
[29]K. Zhang, S. Zhang, A. Rothmayer, and H. Hu, "Development of a digital image projection technique to measure wind-driven water film flows," AIAA Paper No. AIAA 2013-0247, 2013.
[30]K. Zhang, W. Tian, and H. Hu, "An experimental investigation on the surface water transport process over an airfoil by using a digital image projection technique," Exp. Fluids **56**, 173 (2015).
[31]H. Schlichting, K. Gersten, H. Schlichting, and K. Gersten, *Fundamentals of Boundary-Layer Theory* (Springer Berlin Heidelberg, 2000).
[32]C. P. Gendrich and M. M. Koochesfahani, "A spatial correlation technique for estimating velocity fields using molecular tagging velocimetry (MTV)," Exp. Fluids **22**, 67 (1996).
[33]L. Gao, R. Veerakumar, Y. Liu, and H. Hu, "Quantification of the 3D shapes of the ice structures accreted on a wind turbine airfoil model," J. Visualization **22**, 661 (2019).
[34]A. D. D. Craik, "Wind-generated waves in thin liquid films," J. Fluid Mech. **26**, 369 (1966).